

# A Practical Approach to Coronal Magnetic Field Extrapolation Based on the Principle of Minimum Dissipation Rate

Qiang Hu and B. Dasgupta

Institute of Geophysics and Planetary Physics, University of California, Riverside, CA  
92521

qiang.hu@ucr.edu

D. P. Choudhary

Department of Physics and Astronomy, California State University, Northridge, CA 91330

and

J. Büchner

Max-Planck-Institut für Sonnensystemforschung, Max-Planck-Str. 2, 37191,  
Katlenburg-Lindau, Germany

Received \_\_\_\_\_; accepted \_\_\_\_\_

to be submitted

## ABSTRACT

We present a newly developed approach to solar coronal magnetic field extrapolation from vector magnetograms, based on the Principle of Minimum Dissipation Rate (MDR). The MDR system was derived from a variational problem that is more suitable for an open and externally driven system, like the solar corona. The resulting magnetic field equation is more general than force-free. Its solution can be expressed as the superposition of two linear (constant- $\alpha$ ) force-free fields (LFFFs) with distinct  $\alpha$  parameters, and one potential field. Thus the original extrapolation problem is decomposed into three LFFF extrapolations, utilizing boundary data. The full MDR-based approach requires two layers of vector magnetograph measurements on solar surface, while a slightly modified practical approach only requires one. We test both approaches against 3D MHD simulation data in a finite volume. Both yield quantitatively good results. The errors in the magnetic energy estimate are within a few percents. In particular, the main features of relatively strong perpendicular current density structures, representative of the non-force freeness of the solution, are well recovered.

*Subject headings:* MHD — methods: data analysis — Sun: corona — Sun: magnetic fields

## 1. Introduction

Plasma relaxation processes are ubiquitous in astrophysical and laboratory plasmas. One well-known approach is to invoke the variational principle, minimizing the total magnetic field energy subject to the constraint of constant total magnetic helicity (Taylor 1974). Such an approach yields the magnetic field equation for a relaxed plasma state, in which the Lorentz force vanishes, i.e., the so-called linear force-free field (LFFF) with a constant  $\alpha$  parameter,

$$\nabla \times \mathbf{B} = \alpha \mathbf{B}. \quad (1)$$

Although the above equation (1) has been widely applied in modeling magnetic field configurations in laboratory plasma devices and in solar atmosphere, it is found inadequate in certain situations (e.g., Gary 2001; Metcalf et al. 1995). In particular, Amari & Luciani (2000), among others, showed by 3D numerical MHD simulation that in certain solar physics situation, after initial helicity drive, the final “relaxed state is far from the constant- $\alpha$  linear force-free field that would be predicted by Taylor’s conjecture” with helicity conserved. They suggested to derive alternative variational problem.

An alternative approach, also based on the variational principle, was recently developed for an open system with external drive, and applied to theoretical investigation of the solar arcade structures with flow (Bhattacharyya & Janaki 2004; Bhattacharyya et al. 2007). It was later applied to develop a new approach to the extrapolation of solar coronal magnetic field in non-force free state (Hu & Dasgupta 2006, 2007; Hu et al. 2007). The core of the approach is to construct a variational problem based on the Principle of Minimum Dissipation Rate (MDR), which states “The steady state of an irreversible process is characterized by a minimum value of the rate of entropy production” (Prigogine 1947). In most cases, the entropy production rate is equivalent to the energy dissipation rate. The basis is the set of generalized momentum balance equations, and

the system, with flow, is always in broadly-defined force-balanced dynamic equilibrium, satisfying the MHD equations (Bhattacharyya & Janaki 2004). Prior works based on MDR (Montgomery & Phillips 1988; Dasgupta et al. 1998, 2002) had successfully shown that it was able to yield a pressure-balanced configuration, supporting a finite plasma pressure gradient found in plasma confinement devices. Recently a proof of MDR was rigorously sought by 3D numerical simulations (Shaikh et al. 2007). We refer the readers to the above referenced literatures for detailed description and justification of the theoretical basis of MDR.

In short, analogous to the principle of minimum energy, but for a more complex, open system like the solar corona, the MDR yields the following equations for the magnetic field  $\mathbf{B}$  and flow vorticity  $\vec{\omega} = \nabla \times \mathbf{v}$ ,  $\mathbf{v}$  being the plasma flow velocity (Bhattacharyya & Janaki 2004; Bhattacharyya et al. 2007; Hu & Dasgupta 2007):

$$\nabla \times \nabla \times \mathbf{B} + a_1 \nabla \times \mathbf{B} + b_1 \mathbf{B} = \nabla \psi, \quad (2)$$

$$\nabla \times \nabla \times \vec{\omega} + a_2 \nabla \times \vec{\omega} + b_2 \vec{\omega} = \nabla \chi. \quad (3)$$

Here, coefficients  $a$  and  $b$  are constants, and involve the parameters of the system. The right-hand sides of both equations are arbitrary, undetermined functions.

In what follows, we first briefly provide a heuristic justification of the MDR in Section 2, based on a simple but standard analysis. We then present a brief but comprehensive description of the full MDR-based coronal magnetic field extrapolation approach in Section 3, including a new test case study utilizing 3D MHD simulation data of a bright point region, highlighting the non-force free features of the solution. In Section 4, we develop a practical approach that requires only one single-layer vector magnetogram and show that it achieves the same satisfactory results as the full approach for the same test case. In the last Section 5, we conclude and discuss the significance and limitations of our approach.

## 2. Heuristic Justification of the MDR

In a generally resistive plasma, the Lundquist number,  $S$ , is defined as the ratio of the resistive time scale over the Alfvén time scale,  $S = \frac{\tau_R}{\tau_A}$  (e.g., Ortolani & Schnack 1993). The Lundquist number scales with  $L_0/\eta_0$ , the ratio of the characteristic length over the resistivity of the system. Therefore the number  $S$  can be very large when  $L_0$  is large and/or plasma is highly conductive ( $\eta_0$  is small). For example, it can reach  $\sim 10^6 - 10^8$  in a hot fusion plasma, while for solar coronal structures it often exceeds  $10^{12}$ .

From standard procedures (e.g., Ortolani & Schnack 1993), the decay rates of global magnetic helicity,  $K$ , and magnetic energy,  $W$ , are given as follows (with the magnetic field being Fourier decomposed as  $\mathbf{B} = \sum_{\mathbf{k}} \mathbf{b}_{\mathbf{k}} \exp(i\mathbf{k} \cdot \mathbf{r})$ ):

$$\begin{aligned} \frac{dK}{dt} &= -\frac{2\eta}{S} \int_V \mathbf{j} \cdot \mathbf{B} dV \sim -\frac{2\eta}{S} \sum_k k b_k^2, \\ R = \frac{dW}{dt} &= -\frac{\eta}{S} \int_V j^2 dV \sim -\frac{\eta}{S} \sum_k k^2 b_k^2. \end{aligned}$$

Taylor envisioned the relaxation process occurring as a result of small scale turbulence, with  $S \gg 1$ . Following Ortolani & Schnack (1993), at scale lengths for which the Fourier decomposition wavenumber  $k$  is  $\sim S^{1/2}$ , the energy decay  $dW/dt$  is  $\sim O(1)$ . But for such scale length, the helicity decay rate  $dK/dt$  is  $\sim O(S^{-1/2}) \ll 1$ . Thus, from this heuristic argument, we may expect that small scale turbulence dissipate energy at a greater rate than helicity. In the same way, we can show that  $dR/dt \sim -\frac{2\eta^2}{S^2} \sum_k k^4 b_k^2$  goes at a much faster rate than  $dK/dt$ . Furthermore, a recent 3D time-dependent simulation of MHD fluids proves this argument (Shaikh et al. 2007). It is shown that the energy dissipation rate,  $\int \eta j^2 dV$ , decays the fastest towards a minimum state. We again refer readers to Shaikh et al. (2007) for a complete description of the 3D numerical simulation results.

### 3. The Full MDR-Based Approach to Coronal Magnetic Field Extrapolation

The full MDR-based approach to coronal magnetic field extrapolation has been developed and tested against analytic models in Hu & Dasgupta (2007); Hu et al. (2007), based on the general equation yielded from MDR. The following equation results by taking an extra curl on both sides of Eq. (2):

$$\nabla \times \nabla \times \nabla \times \mathbf{B} + a_1 \nabla \times \nabla \times \mathbf{B} + b_1 \nabla \times \mathbf{B} = 0. \quad (4)$$

The aim is to solve the above equation in a finite volume utilizing boundary data. The key is that one exact solution to Eq. (4) exists and can be expressed as the superposition of three LFFFs. Each satisfies Eq. (1) with distinct  $\alpha$  parameters. For the sake of completeness, we briefly reiterate the procedures of the full approach in the following subsection.

#### 3.1. Procedures

The exact solution to Eq. (4) is written

$$\mathbf{B} = \mathbf{B}_1 + \mathbf{B}_2 + \mathbf{B}_3, \quad (5)$$

with  $\nabla \times \mathbf{B}_i = \alpha_i \mathbf{B}_i$ ,  $i = 1, 2, 3$ . Subsequently, one obtains (taking curls on both sides of Eq. (5))

$$\begin{pmatrix} \mathbf{B} \\ \nabla \times \mathbf{B} \\ \nabla \times \nabla \times \mathbf{B} \end{pmatrix} = \mathcal{V} \begin{pmatrix} \mathbf{B}_1 \\ \mathbf{B}_2 \\ \mathbf{B}_3 \end{pmatrix},$$

where the matrix  $\mathcal{V}$  is a (transposed) Vandermonde matrix composed of constant elements  $\alpha_i^{j-1}$ ,  $i, j = 1, 2, 3$ . It is guaranteed invertible provided that the parameters  $\alpha_i$ ,  $i=1,2,3$ , are

distinct. Therefore, it follows

$$\begin{pmatrix} \mathbf{B}_1 \\ \mathbf{B}_2 \\ \mathbf{B}_3 \end{pmatrix} = \mathcal{V}^{-1} \begin{pmatrix} \mathbf{B} \\ \nabla \times \mathbf{B} \\ \nabla \times \nabla \times \mathbf{B} \end{pmatrix}. \quad (6)$$

The above equations provide the bottom boundary condition for each LFFF  $\mathbf{B}_i$ , given vector magnetograph measurements  $\mathbf{B}$  at certain bottom levels on the solar surface. In order to evaluate the double-curl term at the bottom boundary, ideally at least two levels of vector magnetograms have to be utilized and only the normal component of  $\mathbf{B}_i$  perpendicular to the bottom boundary can be obtained (Hu & Dasgupta 2007). Then each LFFF  $\mathbf{B}_i$  is extrapolated into a finite volume above the bottom boundary using the FFT-based method by Alissandrakis (1981) with known  $\alpha_i$  parameters for a Cartesian geometry. The summation of the three LFFFs yields the final solution according to Eq. (5), a non-force free field in general.

It turns out that one of the  $\alpha_i$  has to be zero and the corresponding  $\mathbf{B}_i$  becomes potential. The reason is simply that the solution (5) has to satisfy Eq. (4) (see Hu & Dasgupta 2007; Hu et al. 2007, and Section 4). We arbitrarily choose  $\alpha_2 = 0$ , then  $a_1 = -(\alpha_1 + \alpha_3)$  and  $b_1 = \alpha_3\alpha_1$ .

The determination of  $\alpha_1$  and  $\alpha_3$  is by trial-and-error: enumerate all possible pairs of  $\alpha_1$  and  $\alpha_3$ , preferably within the limit of  $\alpha_{max}$  (Gary 1989), for each pair and  $\alpha_2 \equiv 0$ , solve for the transverse field  $\mathbf{b}_{it}$  at the bottom boundary only, then evaluate the deviation between the “exact” (measured)  $\mathbf{B}_t$  and  $\mathbf{b}_t = \sum_{i=1}^3 \mathbf{b}_{it}$  by (e.g., Schrijver et al. 2006)

$$E_n = \sum_{i=1}^M |\mathbf{B}_{t,i} - \mathbf{b}_{t,i}| / \sum_{i=1}^M |\mathbf{B}_{t,i}|, \quad (7)$$

where  $M = N^2$ , the total number of grids on the transverse plane, and the optimal pair  $(\alpha_1, \alpha_3)_{opt}$  is chosen such that the corresponding  $E_n^{opt}$  is minimum.

To summarize, the procedures of the full MDR-based approach to coronal magnetic field extrapolation constitute the following two steps:

1. Set  $\alpha_2 = 0$  and search through LFFF parameters,  $\alpha_1$  and  $\alpha_3$  ( $\alpha_1 > \alpha_3$ , due to the exchangeability of subscripts, 1 and 3). Apply an LFFF solver to calculate the transverse components  $\mathbf{b}_{it}$ , utilizing the normal component  $B_{in}$  (given by equations (6)),  $i = 1, 2, 3$ , at bottom boundary only. A pair of optimal  $\alpha_i, i = 1, 3$ , is found, for which the  $E_n$ , given by Eq. (7), is minimum. A plot of  $E_n$  distribution over the  $(\alpha_1, \alpha_3)$  parameter space is prepared to show the goodness and uniqueness of the solution.
2. Solve for  $\mathbf{B}_1$  and  $\mathbf{B}_3$  in a finite volume above the bottom boundary, for the optimal  $\alpha_1$  and  $\alpha_3$  found in Step 1, respectively, and the potential field  $\mathbf{B}_2$  as well. Obtain  $\mathbf{B} = \mathbf{B}_1 + \mathbf{B}_2 + \mathbf{B}_3$  (Eq. (5)).

The run time of the approach based on the FFT algorithm solving each LFFF is approximately in the order of  $P \cdot N^2 \log_2 N$ , largely dependent on the number of search grids,  $P$ , on  $(\alpha_1, \alpha_3)$  in Step 1. However, this process can be easily parallelized by simply dividing the search domain into individual pieces and assigning each piece to a separate processor. One can also start with a coarse grid, then allocate a small but finer grid around a minimum, thus the total number of iterations can be effectively reduced.

### 3.2. A Test Case Study Using Numerical Simulation Data

Several analytic solutions have been utilized to test the full approach outlined in the previous subsection and the results showed the approach was able to recover the solution in a finite volume to certain degree of satisfactory accuracy for several cases (Hu & Dasgupta 2007; Hu et al. 2007). Here in order to simulate a case of real magnetograph measurements



as closely as possible, we employ 3D MHD simulation data surrounding a region of an X-ray Bright Point (BP) (Brown et al. 2001) from Büchner & Nikutowski (2005) (see also, Otto et al. 2007; Büchner 2005, 2006). The simulation started with actual solar magnetic field measurements, and was continuously driven by photospheric motion inferred from solar observations.

The data were provided in a finite Cartesian volume,  $x \times y \times z = 128 \times 128 \times 63$ , with  $z$  being the vertical dimension along the normal direction, at one chosen moment during the 3D dynamic MHD simulation. The bottom two layers of vector magnetic field data are utilized to generate the bottom boundary ( $z = 0$ ) conditions by Eqs. (6). The two steps are carried out as described in Section 3.1. The distribution of  $E_n$  in  $(\alpha_1, \alpha_3)$  parameter space is shown in Figure 1. The minimum value is  $E_n^{opt} \approx 0.30$ , with corresponding  $(\alpha_1, \alpha_3)_{opt} \approx (0.00156, 0.000779)$  (dimensionless), as denoted by the + sign in Figure 1. Fairly significant amount of uncertainty associated with this optimal pair exists. However, further analysis shows that choosing any other pair of  $(\alpha_1, \alpha_3)$  within the innermost contour does not significantly change the extrapolation results. Such similar pattern and small  $\alpha$  values were also observed in Hu & Dasgupta (2007).

The corresponding optimal transverse magnetic field vectors  $\mathbf{b}_t$  at  $z = 0$ , are shown in Figure 2, together with the “exact” solution  $\mathbf{B}_t$  from the simulation data and the corresponding potential field results using the normal component  $B_z$  only (Venkatakrishnan & Gary 1989). Our solution agrees very well with the “exact” one, whereas the potential field result exhibits apparent deviations.

The final extrapolation results are shown in Figure 3, in the form of 3D field line plots. The bottom image shows the normal component distribution at  $z = 0$ , with two major polarities in the center corresponding to the location of BP. The field lines from our result demonstrate a good deal of similarity (nearly identical in the upper left part) to the “exact”

solution, indicating good-quality recovery of the magnetic field in the finite volume from the bottom two layers of data. This judgement is supported by the set of quantitative measures, so-called figures of merit, adopted from Schrijver et al. (2006), given in Table 1. They are used to evaluate, quantitatively, the agreement between the exact vector field  $\mathbf{B}$  and the corresponding extrapolated field  $\mathbf{b}$  in a volume (columns 2-5). The 2nd row in Table 1 lists the numbers for this calculation (result 1), and the last two rows list the values for a result identical to the exact solution and a potential field extrapolation, respectively. The last two columns show the energy estimates, the magnetic energy ratio of the extrapolated field  $\mathbf{b}$  over the exact field  $\mathbf{B}$ , i.e.,  $\epsilon = \mathbf{b}^2/\mathbf{B}^2$ , and the energy ratio,  $\epsilon_p$ , that of  $\mathbf{b}$  over the corresponding potential field. For this case, several figures from the potential field extrapolation are comparable with our results. However, the energy estimates clearly mark the distinction: ours only differs from the exact ones by  $\sim -1\%$ , whereas the potential field results differ by as large as  $\sim -16\%$ .

To further characterize the non-force freeness of the solution, which cannot be captured by either the potential or the force-free extrapolation, and to better visualize the results, we calculate the field-line integrated current density,  $J = \int j dl$ , along individual field lines (e.g., Büchner 2006). Figure 4 shows such quantity separated into field-aligned ( $\parallel \mathbf{B}$ ) component,  $J_{\parallel}$ , and the component perpendicular to  $\mathbf{B}$ ,  $J_{\perp}$ , for the “exact” solution. A non-vanishing  $J_{\perp}$  indicates the field is non-force free. Two footpoints of one single field line, both rooted on the bottom boundary, have the same value. Figure 5 shows the corresponding  $J_{\parallel}$  and  $J_{\perp}$  for our result 1 discussed above. The distribution of  $J_{\parallel}$  is well recovered with concentrations at the two major polarities around the center. The major features of  $J_{\perp}$  at the same locations are well recovered as well, but most of the remaining weak structures are lacking, compared with the right panel in Figure 4. However, both  $J_{\perp}$  and  $J_{\parallel}$  enhancements near the lower boundary tracing back to one of the strong polarities to the right, remain. It is indicative of strong currents, implying the possible locations of

current sheets that are important for magnetic reconnection (Büchner 2005, 2006).

At present time, multiple ( $\geq 2$ ) layers of vector magnetograms are hardly available (but see, e.g., Metcalf et al. 1995). Only the photospheric vector magnetic fields are routinely observed. Sometimes, the chromospheric magnetic field line-of-sight (LOS) components were inferred (e.g., Choudhary et al. 2001). When the observations are near the disk center, the LOS component can be used as the normal component  $B_z$ , then the term  $(\nabla \times \nabla \times \mathbf{B})_z = -\nabla^2 B_z$  may be approximated by (denoting the distance between the chromosphere and the photosphere by  $\Delta z$ ),

$$\nabla^2 B_z \approx \nabla_t^2 B_z + 2(B_z^{chrom} - B_z^{photo} - \frac{\partial B_z}{\partial z} \Delta z) / \Delta z^2. \quad (8)$$

The first-order derivative  $\partial B_z / \partial z$  is approximated by the divergence free condition using transverse magnetic field vectors at the photosphere. The 3rd row of Table 1 (result 2) lists the figures of merit of the extrapolation result using the bottom boundary magnetic field vectors and only the  $B_z$  component at one level immediately above to approximate  $\nabla^2 B_z$  by Eq. (8). It shows somewhat deteriorated results, and the error in energy estimate is  $\sim +12\%$ .

#### 4. A Practical Approach Utilizing Single-Layer Vector Magnetogram

As mentioned earlier, the multi-layer vector magnetograms are not routinely available. On the other hand, the high-quality photospheric vector magnetograms become increasingly available. In order to apply our method to actual measurements currently available, we adapt our approach to employ only one single layer vector magnetogram, at the expense of less-general, expected limited applications, as to be described below.

From Eq. (2), considering the arbitrary nature of  $\nabla\psi$ , one may write one exact solution

to (2),

$$\mathbf{B} = \mathbf{B}_1 + \mathbf{B}_3 + c\mathbf{B}_{pot}, \quad (9)$$

where a constant,  $c$ , and the potential field,  $\mathbf{B}_{pot}$ , obtained from the known normal field  $B_z$  at the bottom boundary, are introduced. Then it follows  $\nabla\psi = b_1 c\mathbf{B}_{pot}$ . This is equivalent to the full approach in Section 3, except that the potential field  $\mathbf{B}_2$  is chosen a special form,  $c\mathbf{B}_{pot}$ , and is largely known subject to a undetermined constant.

With an additional unknown parameter,  $c$ , the procedures are similar to those outlined in Section 3.1, but for a reduced, 2nd order system. The following equations, in place of (6), now provide the bottom boundary conditions for each LFFF from one single layer vector magnetogram:

$$\begin{aligned} (\alpha_3 - \alpha_1)B_{1z} &= \alpha_3 B'_z - (\nabla \times \mathbf{B})_z, \\ (\alpha_1 - \alpha_3)B_{3z} &= \alpha_1 B'_z - (\nabla \times \mathbf{B})_z, \end{aligned}$$

with  $B'_z = B_z - cB_{pot,z}$ . In addition to the  $(\alpha_1, \alpha_3)$  search domain in Step 1, another dimension in  $c$  is added. A desirable choice of allowable  $c$  values is  $c \in [-1, 1]$ , to limit the dominance of the potential field. The approach first reported in Hu & Dasgupta (2006) represents the special case,  $c \equiv 0$ .

We again test this practical approach against the same data set utilized in Section 3, but only use the vector magnetic field data on the bottom boundary,  $z = 0$ . Only a limited number of  $c$  values are chosen,  $c \in [-1, -0.5, 0, 0.5, 1]$ . The  $E_n$  distribution at  $c_{min} = -1.0$ , which yields the minimum,  $E_n^{opt} \approx 0.22$ , is shown in Figure 6. Compared with Figure 1, the uniqueness of  $(\alpha_1, \alpha_3)_{opt}$  is much improved. The corresponding  $\mathbf{b}_t$  at  $z = 0$ , and the 3D field line plot are shown in Figures 7 and 8, respectively. The corresponding figures of merit are given in the 4th row (result 3) of Table 1. Good agreement with the exact solution is achieved. The energy estimate has a  $\sim -5\%$  error. The field-line-integrated current

densities shown in Figure 9 are essentially the same as the previous ones obtained by the full approach. All the main features discussed in Section 3.2 are retained.

## 5. Conclusions and Discussion

In conclusions, we develop an approach to extrapolate the coronal magnetic field from vector magnetograms based on the Principle of Minimum Dissipation Rate (MDR). Analogous to, but yet opposed to the principle of minimum energy, the MDR yields a generally non-force free magnetic field through a different variational approach. The full MDR-based approach requires two layers of vector magnetograms, while a practical approach, representing a class of special solutions to the MDR system, requires only one layer, which is more amiable for practical applications to currently available data. A test case study using numerical simulation data shows that both approaches recover the solution to a good degree of accuracy, as measured by a set of quantitative measures. The errors in energy estimate are both within a few percents. Moreover, the non-force free features of the solution, mainly the strong perpendicular current density concentrations, are well retained in the extrapolation results as well.

We hereby provide an alternative approach that is fast, and easy to implement, and allows one to extrapolate coronal magnetic field in a more general non-force free state with manageable effort in a solo work. For instance, all the calculations reported herein ( $128 \times 128 \times 63$  grid) were performed on a single-processor 2.8GHz PC in IDL within a reasonable time frame. It potentially can be made much faster. It is apparent that the Eq. (4) includes solutions to LFFF ( $\nabla \times \mathbf{B} = \alpha \mathbf{B}$ ), for  $-\alpha_1 = \alpha_3 = \alpha$ . It is not explicit whether this is also the case for the nonlinear force-free field (NLFFF) when the parameter  $\alpha$  is allowed to vary, although several numerical experiments indicated that this might be so (Hu & Dasgupta 2007) sometimes.

We are fully aware of the limitations of the method, due to the fact that the currently employed LFFF solver originates from an ill-posed problem. It is adversely affected by the increasing resolution of vector magnetograms since  $\alpha_{max}$  is inversely proportional to  $N$ . This severely limits the search domain of  $\alpha_i$  that will yield unique physical solutions (e.g., Alissandrakis 1981; Gary 1989). Recent progresses in the algorithm for NLFFF extrapolations (e.g., Song et al. 2006), in addition to the existing LFFF algorithm (e.g., Abramenko & Yurchishin 1996), that modified the problem into a well-posed one, look promising and may be adapted.

It is worth noting that our approach is wholly applicable to extrapolating the plasma flow field, by simply replacing magnetic field  $\mathbf{B}$  with flow vorticity  $\vec{\omega}$ . However the boundary conditions are probably harder to obtain since it is the vorticity that is involved. A good start is to utilize the flow field data contained in the same 3D MHD simulation test case. It is not straightforward to obtain the plasma state since the flow field has to be resolved as well, and to be consistent, the full set of MHD equations has to be considered (see, e.g., Montgomery & Phillips 1988). One may also foresee that extension of this approach to the whole solar surface data is of great significance. Further theoretical investigation is underway.

We are grateful to Drs. D. Shaikh, M.S. Janaki, and R. Bhattacharyya for useful discussions. HQ and BD acknowledge NASA LWS grant NNX07A073G for partial support.

## REFERENCES

- Abramenko, V.I., & Yurchishin, V. 1996, Sol. Phys., 168, 47
- Alissandrakis, C.E. 1981, A&A, 100, 197
- Amari, T., & Luciani, J. F. 2000, Phys. Rev. Lett., 84, 1196
- Bhattacharyya, R., Janaki, M.S., Dasgupta, B., & Zank, G. 2007, Sol. Phys., 240, 63
- Bhattacharyya, R., & Janaki, M.S. 2004, Phys. Plasmas, 11, 5615
- Brown, D.S. et al., 2001, Sol. Phys., 201, 305
- Büchner, J. 2006, Space Sci. Rev., 122, 149
- Büchner, J., & Nikutowski, B. 2005, Procs. of the International Scientific Conference on Chromospheric and Coronal Magnetic Fields, ESA SP-596
- Büchner, J. 2005, Procs. of the 11th European Solar Physics Meeting, ESA SP-600
- Choudhary, D.P., Sakurai, T., & Venkatakrishnan, P. 2001, ApJ, 560, 439
- Dasgupta, B., Dasgupta, P., Janaki, M.S., Watanabe, T., & Sato, T. 1998, Phys. Rev. Lett., 81, 3144
- Dasgupta, B., Janaki, M.S., Bhattacharyya, R., Dasgupta, P., Watanabe, T., & Sato, T. 2002, Phys. Rev. E, 65, 046405.
- Gary, G.A. 1989, ApJS, 69, 323
- Gary, G. A. 2001, Sol. Phys., 203, 71
- Hu, Q., & Dasgupta, B. 2006, Geophys. Res. Lett., 33, L15106
- Hu, Q., & Dasgupta, B. 2007, Sol. Phys., submitted

- Hu, Q., Dasgupta, B., & Choudhary, D.P. 2007, AIP CP932, 376
- Metcalf, T. R. et al., 1995, ApJ, 439, 474
- Montgomery, D., & Phillips, L. 1988, Phys. Rev. A, 38, 2953
- Ortolani, S., & Schnack, D.D. 1993, Magnetohydrodynamics of Plasma Relaxation, World Scientific Publishing, Singapore.
- Otto, A., Büchner, J., & Nikutowski, B. 2007, A&A, 468, 313
- Prigogine, I. 1947, *Etude Thermodynamique des Phénomènes Irréversibles*, Edition Desoer, Liège.
- Schrijver, C.J. et al. 2006, Sol. Phys., 235, 161
- Shaikh, D., Dasgupta, B., Zank, G., & Hu, Q. 2007, Phys. Plasmas, submitted
- Song, M.T., Fang, C., Tang, Y., Wu, S.T., & Zhang, Y. 2006, ApJ, 649, 1084
- Taylor, J. B. 1974, Phys. Rev. Lett., 33, 1139
- Venkatakrishnan, P., & Gary, G. A. 1989, Sol. Phys., 120, 235



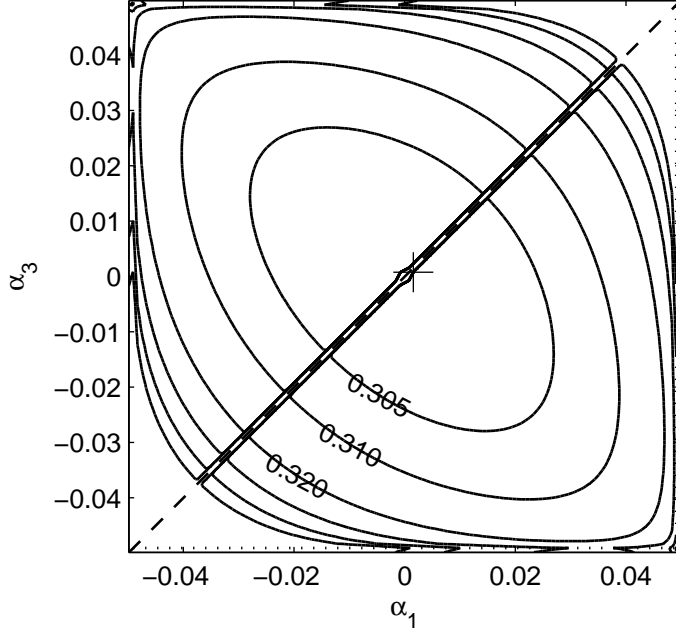


Fig. 1.— Contours of  $E_n$  over the  $(\alpha_1, \alpha_3)$  parameter space for the full MDR-based approach. The unlabeled contour lines are of increment 0.01. The dotted lines mark the limit where  $|\alpha_{1,3}| = \alpha_{max} = 2\pi/N$ . The plus sign denotes the location where  $E_n$  is minimum. Due to the interchangeability of  $\alpha_1$  and  $\alpha_3$ , the plot is symmetric about the dashed line,  $\alpha_1 = \alpha_3$ .

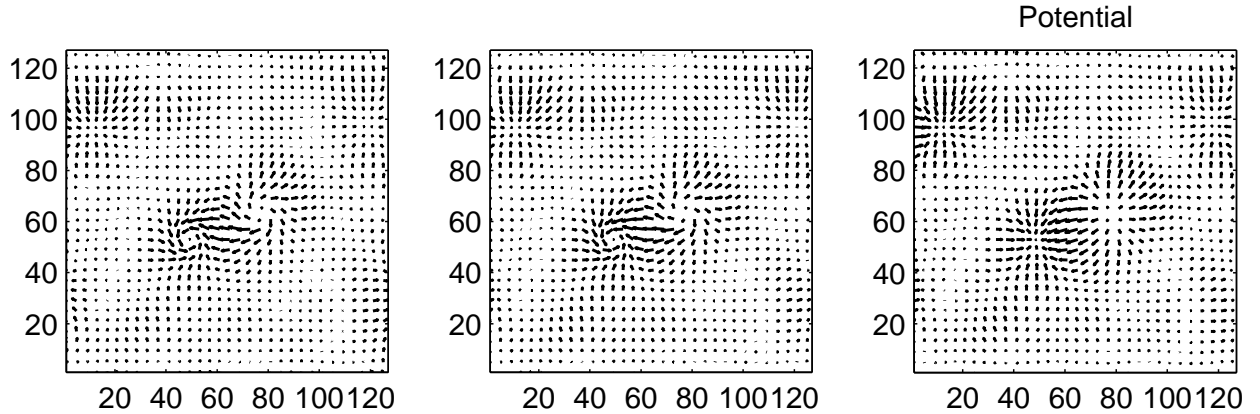


Fig. 2.— The transverse magnetic field vectors at  $z = 0$ . *Left*: The exact distribution from numerical simulation data. *Middle*: The derived optimal result from the full MDR-based approach. *Right*: The result from a corresponding potential field extrapolation.

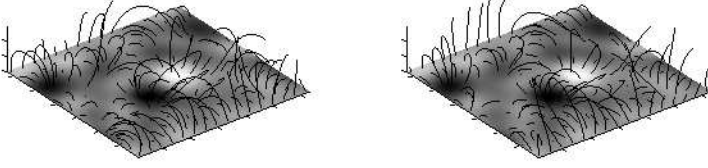


Fig. 3.— 3D field line plots of the exact solution (left panel) and the corresponding extrapolated solution (right panel) from the full MDR-based approach. All the field lines originate from the same set of root points. The bottom image represents the normal magnetic field component distribution on the bottom boundary, with the gray scales ranging from strongly negative (black) to positive (white).

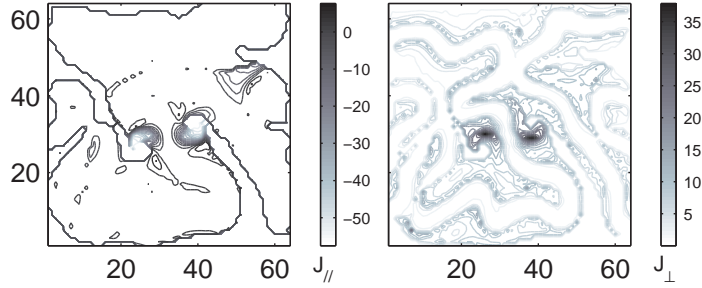


Fig. 4.— Contour plots of field-line-integrated current densities from the exact solution. *Left:* The component parallel to the magnetic field. *Right:* The component perpendicular to the magnetic field. The gray colors show the levels of the contour lines, as indicated by the colorbars.

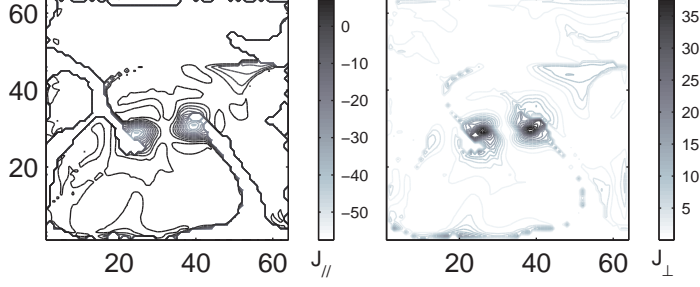


Fig. 5.— The corresponding field-line-integrated current density distributions obtained by the full MDR-based approach. Format is the same as Figure 4. So are the gray scales.

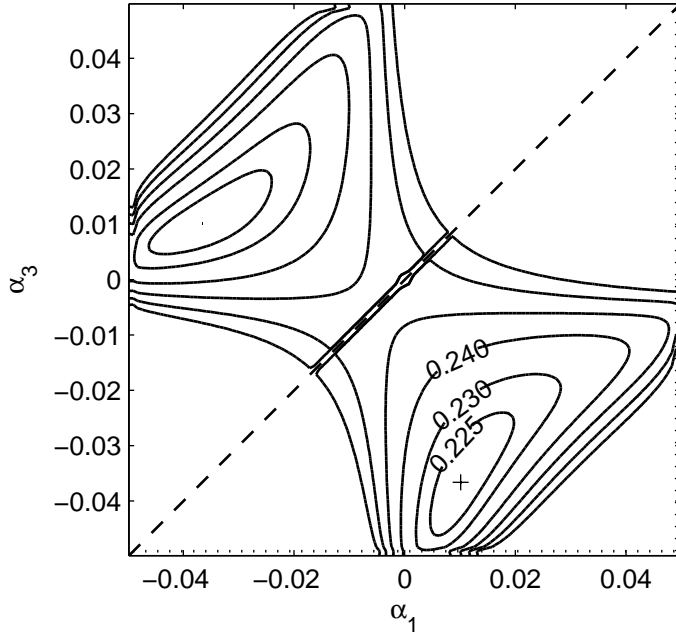


Fig. 6.— The  $E_n$  distribution for the practical MDR-based approach. Format is the same as Figure 1.

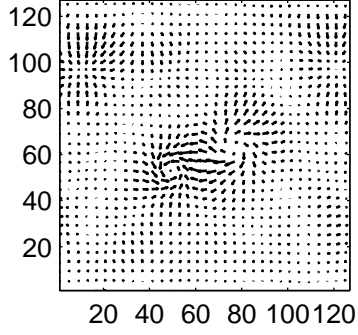


Fig. 7.— The corresponding transverse magnetic field vectors at  $z = 0$ , obtained by the practical approach.

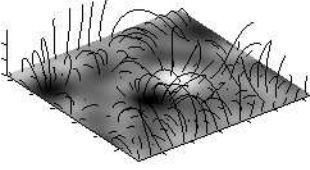


Fig. 8.— The corresponding 3D field line plot, obtained by the practical approach. Format is the same as Figure 3.

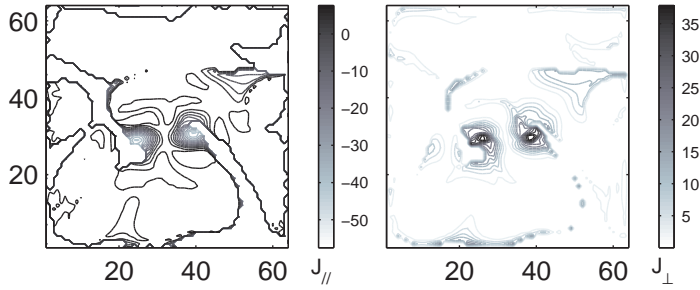


Fig. 9.— The field-line-integrated current densities obtained by the practical approach. Format is the same as Figure 4.

Table 1: Figures of merit (see Schrijver et al. (2006) and text for definitions).

Case BP	$C_{vec}$	$C_{cs}$	$E'_n$	$E'_m$	$\epsilon$	$\epsilon_p$
Our result 1 <sup>a</sup>	0.97	0.91	0.74	0.62	<b>0.99</b>	<b>1.18</b>
Our result 2 <sup>b</sup>	0.91	0.76	0.53	0.27	<b>1.12</b>	<b>1.34</b>
Our result 3 <sup>c</sup>	0.97	0.93	0.76	0.64	<b>0.95</b>	<b>1.14</b>
Exact	1	1	1	1	<b>1</b>	<b>1.20</b>
Potential	0.95	0.92	0.70	0.63	<b>0.84</b>	<b>1.00</b>

---

<sup>a</sup>Results obtained by the full MDR approach (see Section 3), where two bottom layers of vector magnetic field data are utilized to derive the bottom boundary conditions.

<sup>b</sup>Results obtained by the reduced bottom boundary data (see Section 3.2), where only the vector magnetic field on the bottom layer, and the normal magnetic field component on the layer immediately above are utilized.

<sup>c</sup>Results obtained by the practical approach (see Section 4), where only the magnetic field vectors on the bottom boundary are required.